

PAPER • OPEN ACCESS

Determination of acoustic phonon anharmonicities via second-order Raman scattering in CuI

To cite this article: R Hildebrandt *et al* 2023 *New J. Phys.* **25** 123022

View the [article online](#) for updates and enhancements.

You may also like

- [Modeling the contribution of point defects to the Raman spectrum of crystalline materials](#)
Guido Roma
- [Polarization of the first-order Raman spectrum of crystals with the zinc-blende structure \(indium phosphide\)](#)
P H Borchers and G F Alfrey
- [Anomalous multi-order Raman scattering in LaMnO₃: a signature of quantum lattice effects in a Jahn–Teller crystal](#)
N N Kovaleva, O E Kusmartseva, K I Kugel *et al.*



PAPER

Determination of acoustic phonon anharmonicities via second-order Raman scattering in CuI

OPEN ACCESS

RECEIVED

19 September 2023

REVISED

20 November 2023

ACCEPTED FOR PUBLICATION








30 November 2023

PUBLISHED

11 December 2023

Original Content from
this work may be used
under the terms of the
[Creative Commons
Attribution 4.0 licence](#).

Any further distribution
of this work must
maintain attribution to
the author(s) and the title
of the work, journal
citation and DOI.

R Hildebrandt^{1,*} , M Seifert² , J George^{2,3} , S Blaurock⁴, S Botti^{2,5} , H Krautscheid⁴ ,
M Grundmann¹  and C Sturm¹ ¹ Universität Leipzig, Felix Bloch Institute for Solid State Physics, Semiconductor Physics Group, Linnéstraße 5, Leipzig 04103, Germany² Friedrich-Schiller-Universität Jena, Institute of Condensed Matter Theory and Optics, Max-Wien-Platz 1, Jena 07743, Germany³ Federal Institute for Materials Research and Testing Department Materials Chemistry, Unter den Eichen 87, Berlin 12205, Germany⁴ Universität Leipzig, Institute for Inorganic Chemistry, Johannisallee 29, Leipzig 04103, Germany⁵ Ruhr University Bochum, Research Center Future Energy Materials and Systems of the Research Alliance Ruhr, Faculty of Physics and ICAM, Universitätsstraße 150, Bochum 44780, Germany

* Author to whom any correspondence should be addressed.

E-mail: ron.hildebrandt@uni-leipzig.de**Keywords:** density functional theory, acoustic phonons, anharmonicity, second-order Raman scattering, copper iodide, phonon dispersionSupplementary material for this article is available [online](#)**Abstract**

We demonstrate the determination of anharmonic acoustic phonon properties via second-order Raman scattering exemplarily on copper iodide single crystals. The origin of multi-phonon features from the second-order Raman spectra was assigned by the support of the calculated 2-phonon density of states. In this way, the temperature dependence of acoustic phonons was determined down to 10 K. To determine independently the harmonic contributions of respective acoustic phonons, density functional theory in quasi-harmonic approximation was used. Finally, the anharmonic contributions were determined. The results are in agreement with earlier publications and extend CuI's determined acoustic phonon properties to lower temperatures with higher accuracy. This approach demonstrates that it is possible to characterize the acoustic anharmonicities via Raman scattering down to zero-temperature renormalization constants of at least 0.1 cm^{-1} .

1. Introduction

Phonons are collective excitation of condensed matter and specifically for solids of fundamental relevance. They are well-defined for crystal lattices, but as well of relevance for non-crystalline solids. The phonon's origin is bond related and is hence of local nature [1]. This may reveal characteristics, which are otherwise concealed for delocalized properties [1]. Interaction of phonons with other particles are of relevance in low-dimensional materials [2], for electron-phonon coupling in general [2], in phonon reabsorption processes [3] as well as for non-radiative recombination processes [4]. Aside of sound waves, also the transport of heat is mediated via phonons. Here, low thermal conductivity may be used for thermal barriers [5] or as well in thermoelectric applications [6, 7]. These thermal transport properties though, are directly linked to phonon anharmonicities. For a deep understanding of these processes, a precise characterization of general phonon properties is required.

By using optical spectroscopy phonon properties may be investigated. Observed energetic shifts and broadening of phonon modes in dependence on temperature contain information regarding their respective harmonic and anharmonic properties. This covers for example the lattice expansion and phonon decay processes. Using Raman spectroscopy, this type of analysis is a well-known approach for optical zone-center phonons of various materials. Extending this to acoustic phonons is of interest to assign all related processes [8].

By this extension, the need of large neutron scattering facilities to characterize zone-edge phonons would be eliminated. This is demonstrated here by using second-order Raman scattering to characterize acoustic phonons regarding their anharmononicities.

We will show this exemplarily on copper iodide (CuI), which has at room temperature (RT) a zinc blende crystal structure. It is known for its strong anharmonic properties [5, 9, 10], which reflects in CuI's coefficient of thermal conduction, which is as low as $0.5 \text{ W m}^{-1} \text{ K}^{-1}$ and hence the dimensionless figure of merit ZT is about 0.25 [6, 7, 11]. These are promising values for device applications, especially for transparent electronics due to its wide bandgap of 3.1 eV [12] and a hole mobility of up to $43 \text{ cm}^2 \text{ V}^{-1} \text{ s}^{-1}$ [13]. Due to its intrinsic p-type charge carriers, this semiconductor may as well be a suitable complement to the nowadays established wide-bandgap semiconductors ZnO, GaN or SiC, which can be found in high-power or high-frequency applications. CuI has a large exciton binding energy of about 62 meV which makes this promising for opto-electronic applications [12]. Device applications in hetero pn-junctions were demonstrated for solar cells [14], transistors [15] and light emitting diodes [16]. The performance of these different types of electronic and opto-electronic devices is coupled to phonon interactions and especially acoustic phonon properties of interest for thermal or thermoelectric applications.

Information regarding CuI's acoustic phonons is up to now only available via neutron scattering at 90 K and RT [17] and as best of knowledge of the authors, there exist only one short report of the second-order Raman spectrum up to now [18]. The accuracy of 5 cm^{-1} is comparable to reported shifts of phonon energies with temperature. Also a systematic deviation of respective determined acoustic phonons cannot be excluded, as found for the optical zone-center phonons when compared to Raman scattering results [18, 19]. These uncertainties are significant and not addressed despite the recent research interest in this material.

Here we report on the fundamental acoustic phonon properties, which are determined with high accuracy and resolution at high symmetry points. We investigate the temperature behavior and discuss harmonic and anharmonic contributions to the phonon properties. We achieve an energetic accuracy down to 0.3 cm^{-1} and temperatures as low as 10 K, which is a significant improvement compared to available data. The paper is structured as follows: Relevant experimental and computational methods are described in section 2. In section 3 we discuss the phonon assignment and energy shift of the second-order modes, which are then compared to the results of the density functional theory (DFT) calculations. Finally, this is used to analyze the harmonic and anharmonic contributions of acoustic phonons. The results are summarized in section 4.

2. Methods

2.1. Crystal growth and quality

By using copper acetate monohydrate (Sigma-Aldrich, 98%), acetone and iodine (Sigma-Aldrich, 99.5%), copper iodide was synthesized in hot acetic acid. The procedure was similar to the one reported in [20]. The purification of the crude product, carried out by crystallization, was followed by thermal decomposition of an acetonitrile copper iodide complex $[(\text{CH}_3\text{CN})_2(\text{CuI})_2]_n$ [12]. The crystal growth of copper iodide single crystals was realized in autoclaves by taking advantage of the inverse temperature-dependent solubility of copper iodide in acetonitrile [21], similar to the procedure Described in [12]. The resulting γ -CuI bulk crystals were colorless with typical dimensions in the range of 1–4 mm.

The purity of the crystals was determined to be larger than 99.999% with a Bruker S2 Picofox TXRF using a multi-element standard.

Structural characterization of the crystals was done by x-ray diffraction using a PANalytical X'Pert Pro diffractometer with a $\text{Cu K}\alpha$. The crystal facets were (111)-oriented and a cubic lattice constant of $a = 6.053(3) \text{ \AA}$ was determined. ϕ -scans of asymmetrical reflections indicated no twinning or rotational domains of the crystals. Details of the procedures and x-ray diffraction scans can be found in [12].

2.2. Raman scattering

All Raman measurements were performed in a helium flow cryostat (Janis ST-500) with the CuI single crystal fixed on a c-plane sapphire substrate. The temperature was determined by using a calibrated silicon diode mounted on the cold finger. As excitation source we used a 100 mW diode-pumped solid-state laser ($\lambda = 532.06 \text{ nm}$, Coherent Compass 315 M). A Mitutoyo microscope objective with an $NA = 0.42$ was used in a backscattering configuration and a Glan-Thompson prism including a half-wave plate was used to analyze the linear polarization. A double monochromator (Jobin Yvon U1000) with a focal length of $2 \times 1 \text{ m}$ and a $2400 \text{ lines mm}^{-1}$ grating resulted in a spectral resolution of about 0.2 cm^{-1} (CCD: Symphony II BIUV). One measurement window covers a spectral range of about 115 cm^{-1} , with about 17% spectral overlap of two distinct measurements. Rotational Raman lines of air were observed (removed later from spectra) and used for calibration of Raman shift features up to 150 cm^{-1} .

2.3. Computational details

The computations were done in the framework of DFT using the Vienna *ab initio* simulation package VASP [22, 23] with the projector-augmented wave method [24]. The 4s and 3p electrons of Cu and 5s and 5p electrons of I are thereby treated explicitly as valence electrons. Starting with the pure zincblende γ -phase, we used a cutoff energy of 770 eV for the plane-wave basis set and \mathbf{k} -point grid of $8 \times 8 \times 8$. We used here tighter computational settings than in our other studies on CuI [25, 26], to avoid spurious imaginary modes around Γ -point as a potential result of numerical noise [27]. We have applied the exchange–correlation functional PBEsol [28] for structural optimizations and phonon computations. For the full structural optimization with DFT at 0 K, we relaxed all forces until they were smaller than 10^{-5} eV \AA^{-1} . This led to a lattice parameter of 5.940 \AA for PBEsol which is quite close to the experimental value of 6.053 \AA . For the calculation of the Born charges for the non-analytical corrections (NAC), we used a denser \mathbf{k} -point grid of $16 \times 16 \times 16$.

For the phonon calculations, we used the package phonopy [29, 30] together with VASP and computed the harmonic phonons with the help of the finite displacement method with a displacement of 0.01 \AA . We used $4 \times 4 \times 4$ supercells of the primitive cell with a \mathbf{k} -point grid of $2 \times 2 \times 2$ for the computation of the forces. Information on the convergence of the supercell size is given in the supplementary. For the calculation of the 1-Phonon density of states (1PDOS) and the thermal properties, we used a \mathbf{q} -point mesh of $16 \times 16 \times 16$. For the broadening of the 1PDOS, we used a Gaussian smearing with a full-width half maximum (FWHM) of 2 cm^{-1} . To compute the temperature dependence of the phonon modes, we relied on the quasi-harmonic approximation [31]. For this, we chose different volumes roughly around $\pm 10\%$ of the DFT minimum volume. All these cells were relaxed with the constraint to keep the volume constant. We then performed phonon calculations with consistent settings, mentioned above, for these different volumes around the DFT minimum volume to obtain a description of the free energy as a function of volume at different temperatures. Based on this, we obtained the temperature-dependent equilibrium volumes and repeated the phonon calculations at those volumes corresponding to certain temperatures to compare the calculated results with the experimentally derived ones. Further, the obtained results of the phonon properties were compared with the literature to benchmark the chosen parameters and therefore validate these results for the calculation of the 2-phonon density of states. More details regarding this procedure are shown in the supplementary.

The 2-phonon density of states (2PDOS) was obtained out of the phonon frequencies following the equation as defined by [32]:

$$2\text{PDOS}(\vec{q}, j) = 2\pi \sum_{\vec{q}', \vec{q}'', j', j''} \Delta(\vec{q} - \vec{q}' - \vec{q}'') \times \delta(\omega(\vec{q}, j) - \omega(\vec{q}', j') - \omega(\vec{q}'', j'')). \quad (1)$$

$\Delta(\vec{Q})$ is 1, if \vec{Q} is either zero or a multiple of the reciprocal lattice vector. Otherwise $\Delta(\vec{Q})$ is zero. Furthermore, \vec{q} denotes the phonon wave vector, j the corresponding phonon mode and ω the phonon frequency. After evaluating equation (1), just those \vec{q} -points were considered which are located in a small environment around the Γ -point to account for the Raman scattering which is limited to Γ -point. Therefore only \vec{q} -points inside a box of length $2/8|q_{\max}|$ and the Gamma-point in its center were considered. The 2PDOS was broadened with a Gaussian smearing, with a FWHM of 2 cm^{-1} .

3. Results and discussion

3.1. Second-order Raman features

The millimeter-sized single crystals were cooled down to about 10 K and Raman spectra with different integration times in parallel- ($z(xx)\bar{z}$) and cross-polarization ($z(xy)\bar{z}$) were measured to observe the first- and second-order Raman scattering features of CuI.

The first-order spectra can be seen in figure 1(a) and show the transversal optical (TO) and longitudinal optical (LO) mode at 133.3 cm^{-1} and 149.4 cm^{-1} respectively. The second-order Raman signal is shown as well and rescaled by a factor of 300 for clarity. This signal contains four large structures labeled A–D with various features which are listed in detail in table 1. From the phonon dispersion in [17], each structure's origin can be estimated for CuI.

In a second-order Raman process, two phonons are involved in the scattering process. There are three different processes relevant to identify the feature's origin: overtone-, combination- and difference-phonon modes. The overtone process is characterized by a contribution of two phonons from the same phonon branch, with opposite momenta. If their wavenumber is, for example, ω_a , the resulting observed Raman shift is at $2\omega_a$. The phonon combination (+) or difference (–) processes are characterized by two phonons of

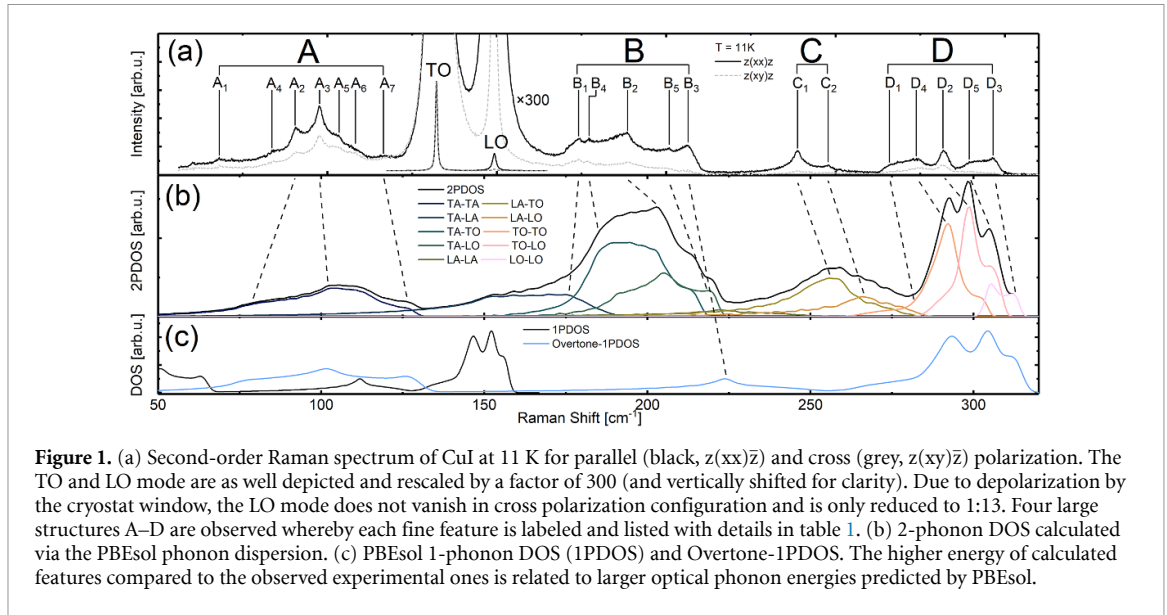


Figure 1. (a) Second-order Raman spectrum of CuI at 11 K for parallel (black, $z(xx)\bar{z}$) and cross (grey, $z(xy)\bar{z}$) polarization. The TO and LO mode are as well depicted and rescaled by a factor of 300 (and vertically shifted for clarity). Due to depolarization by the cryostat window, the LO mode does not vanish in cross polarization configuration and is only reduced to 1:13. Four large structures A–D are observed whereby each fine feature is labeled and listed with details in table 1. (b) 2-phonon DOS calculated via the PBEsol phonon dispersion. (c) PBEsol 1-phonon DOS (1PDOS) and Overtone-1PDOS. The higher energy of calculated features compared to the observed experimental ones is related to larger optical phonon energies predicted by PBEsol.

Table 1. Labels and position of observed Raman features. Assignments of involved phonons are done with the position in the Brillouin zone by critical point labels. Along the Σ -direction, these additional energies were assumed: $LA_{\Sigma} = (LA_X + LA_L)/2 = 114 \text{ cm}^{-1}$, $TA_{\Sigma,l} = (TA_X + TA_L)/2 = 47 \text{ cm}^{-1}$, $TA_{\Sigma,u} = 61 \text{ cm}^{-1}$ and $O_{\Sigma} = (TO_X + LO_X)/2$. The indices ‘l’ and ‘u’ indicate the lower and upper TA phonon branch along the Σ direction. The third column contains the second-order phonon feature energy predicted by our suggested critical point phonon energies from table 2. All energies are given in cm^{-1} .

Label	Experiment (cm^{-1})	Prediction via table 2 (cm^{-1})	Assignment	Point
A ₁	67.5 ^a	67	LA–TA _l	Σ
A ₄	84 ^a	81.5	O–TA _u	Σ
A ₂	90.5	90	2TA	L
A ₃	97.5	98	2TA	X
A ₅	103	—	2TA	K?
A ₆	108	—	2TA	W?
A ₇	>116	122	2TA _u	Σ
B ₁	173.5 ^a	173	TA + LA	X
		175	TA _u + LA	Σ
B ₄	177	181	TA + TO	L
B ₂	188.5	≈190	TA + TO	X
		≈193	TA + LO	X
		190	TA + LO	L
B ₅	200.5	≈ 200	TA _u + O	Σ
B ₃	206	206	2LA	L
C ₁	238.5	238	LA + TO	L
C ₂	247.5	248	LA + LO	L
D ₁	265.5	264.4	2TO	Γ
D ₄	274	270	2TO	L
D ₂	282	280, 285, 281.5	TO + LO	L,X, Γ
		282	2TO	X
D ₅	291	290, 288	2LO	L,X
D ₃	297	298.6	2LO	Γ

^a Also observed in [18].

different phonon branches whereby both phonons have opposite momenta. If their wavenumbers, for example, are ω_a and ω_b , the resulting observed Raman shift is at $\omega_a \pm \omega_b$. Momentum conservation is ensured in each process via opposite momenta of the respective contributing phonons ($q \approx 0$).

We now proceed with discussing our assignment of the observed structures, based on CuI’s known phonon dispersion [17]. The observed structure between 75 cm^{-1} and 120 cm^{-1} (labeled A) were attributed to overtones of transversal acoustic (TA) phonons, whereas the structure between 270 cm^{-1} and 300 cm^{-1}

Table 2. Phonon mode energies at critical points Γ , L and X determined from the second-order Raman scattering spectrum at 9 K. The last columns are our estimated accuracy of the respective energies considering measurement inaccuracies and deviations resulting from the 2PDOS shape. Note that the results from neutron scattering measurements have a significant larger error bar of about $\pm 5 \text{ cm}^{-1}$ [17]. All values are given in cm^{-1} .

Mode	ω_{Γ}	ω_L	ω_X	$\Delta\omega_{\Gamma}$	$\Delta\omega_L$	$\Delta\omega_X$
TA	—	45.3	49.3	—	0.3	0.3
LA	—	103	124	—	2	2
TO	132.2	135	141	0.1	2	4
LO	149.3	145	144	0.1	2	4

(labeled D) are attributed to combinations and overtones of optical phonons. The intermediate structures labeled B ($170\text{--}210 \text{ cm}^{-1}$) and C ($235\text{--}250 \text{ cm}^{-1}$) can be attributed to combinations and overtones of optical and acoustic phonons. For the structure B, mostly TA and optical phonons are involved, while for the structure C, LA and optical phonons participate. Between each structure, a featureless continuum signal is observed. Each feature is here associated with van Hove singularities of the 2PDOS.

The selection rules for second-order Raman processes in zincblende crystals yield that all combinations and overtones are allowed [33] and hence the information of the full phonon dispersion is contained in the second-order Raman spectrum [34–36].

To refine the assignment, we will also include estimates of the intensities from the computed phonon dispersion. The intensity dependence of the individual second-order Raman features is quite complex. It depends upon the phonon dispersion, the second-order Raman susceptibilities of the phonon branches as well as their population. Usually, the spectral shape can be approximated by using the overtone phonon density of states (Overtone-1PDOS), which is the phonon density of states (1PDOS) multiplied by a factor of 2 [34]. This especially emphasizes overtone processes, whereby combination processes are only represented in the 2-phonon DOS (2PDOS, calculated via equation (1)). The 2PDOS and the Overtone-1PDOS are shown in figures 1(b) and (c). Considering both contributions, the origin of each feature can be assigned and, in this way, the individual phonon energies can be derived.

For all observed features, the involved phonons as well as their energy and the corresponding wave vector in the Brillouin zone are summarized in table 2. For TA phonons, the L and X critical points are easily observable, while for the LA phonons the high density of states favors the observation of LA_L related overtones and combinations. Hence, the LA_X mode can be neglected in most cases, because of its low density of states. This is similar to ZnS, which has a quite comparable phonon dispersion compared to CuI [37] due to the relative atomic masses and their high transversal charge values [38]. The LA_L DOS dominance is as well indicated by the phonon dispersion in [39]. This is also supported by a strong parallel-polarized signal at the B_3 feature, which can be a characteristic for overtones [34]. Due to the low dispersion of the optical phonons, all their combinations and overtones are clearly observed as well. In this way, most features were uniquely identified, while only three features were ambiguous.

Deviations from the observed peak position and the phonon energy at the critical point can be seen for example clearly at the D_3 feature. This feature D_3 (297 cm^{-1}) shows a deviation to its LO_{Γ} overtone assignment (298.6 cm^{-1}) by 1.6 cm^{-1} . Deviations of similar magnitude can be observed for other assignments and are usually lower than 2 cm^{-1} . Those deviations can be explained by the different types of maxima involved in the respective 2-phonon scattering transitions and the flatness of the phonon dispersion at respective Brillouin zone points. This would reason a deviation of the 2-phonon density of states maximum [40], compared to the position from the critical points of the phonon dispersion.

From the observed second-order Raman features, the phonon energies at certain critical points in the Brillouin zone were deduced and were given in table 2. Within respective error bars, We observed a good agreement with values determined by neutron scattering [17, 39], whereby our values were determined with much higher precision. For acoustic phonons, only the TA phonon at the L-point was observed at a higher wavenumber. The energetic ordering of the optical phonons at the respective critical points is resembled in addition to assuming a non-crossing behavior of the TO and LO mode, as observed for the phonon dispersions in [39]. This is expected for CuI due to its high transversal charge similar to ZnS [10, 37, 41–43]. The non-crossing, though, is not reproduced by our calculated phonon dispersion. Similar deviations between experimental and calculated phonon dispersion are as well observed for CuBr or ZnTe [37, 39, 44]. Nevertheless, the spectral shape is well resembled by the 2PDOS.

For the optical overtones (structure D), the present crossing of TO and LO phonons in the DFT-based phonon dispersion reasons a weak separation of individual TO-TO (D_1), TO-LO (D_2) and LO-LO (D_3) phonon combinations. This is better represented by the individual parts of the 2PDOS (figure 1(b)).

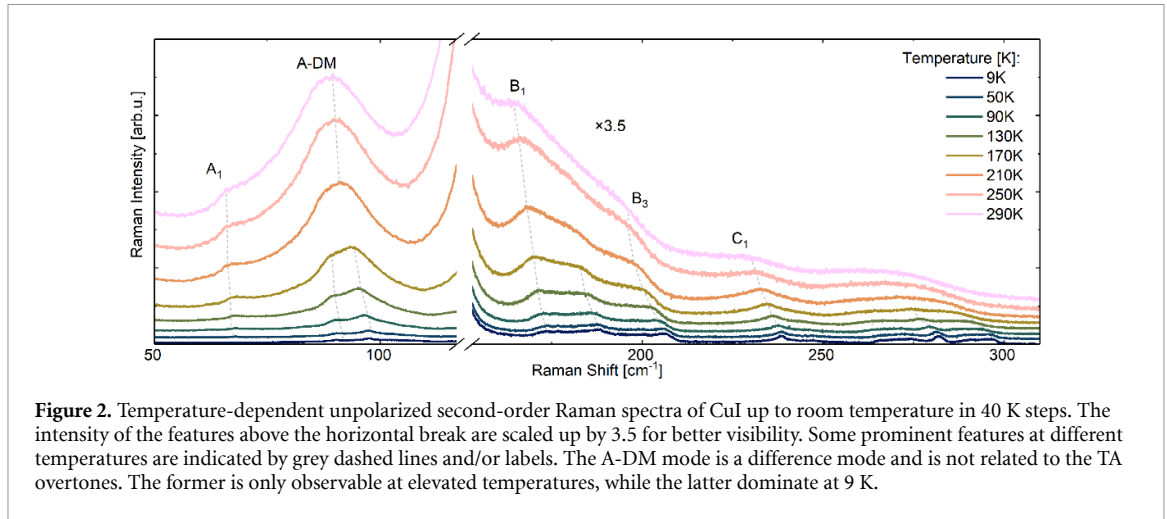


Figure 2. Temperature-dependent unpolarized second-order Raman spectra of CuI up to room temperature in 40 K steps. The intensity of the features above the horizontal break are scaled up by 3.5 for better visibility. Some prominent features at different temperatures are indicated by grey dashed lines and/or labels. The A-DM mode is a difference mode and is not related to the TA overtones. The former is only observable at elevated temperatures, while the latter dominate at 9 K.

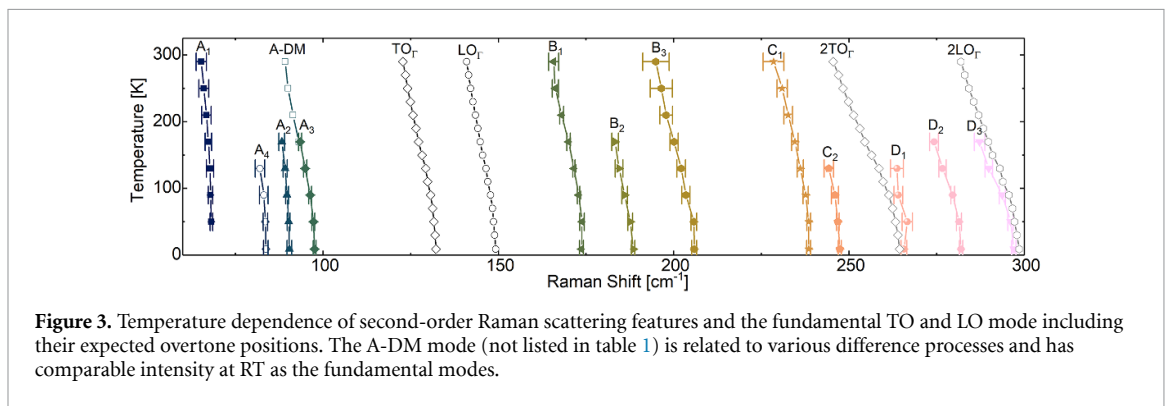


Figure 3. Temperature dependence of second-order Raman scattering features and the fundamental TO and LO mode including their expected overtone positions. The A-DM mode (not listed in table 1) is related to various difference processes and has comparable intensity at RT as the fundamental modes.

3.2. Temperature dependence of Raman modes

The identified features in the second-order Raman spectrum at low temperature were related to the combinations, differences and overtones of various acoustic and optical phonon modes. With increasing temperature a Raman shift to lower wavenumbers of the features is observed in addition to a strong increase of broadening. This restricts the number of traceable features at elevated temperatures. The measured Raman spectra as a function of temperature are shown in figure 2.

The intensity of the structures B, C and D rises with increasing temperature according to $I_{\text{sum}} \propto [n(\omega_a) + 1][n(\omega_b) + 1]$, as expected for overtone and combinations modes [45, 46]. Here $n(\omega_i) = [\exp(\hbar c \omega_i / k_B T) - 1]^{-1}$ is the Bose–Einstein distribution function with ω_i the wavenumber of the phonon. For the structure A at elevated temperatures, an additional contribution from a difference mode has to be considered, i.e. $I_A \propto I_{\text{sum}} + [n(\omega_c) + 1][n(\omega_d)]$ with $\omega_c - \omega_d \approx 90 \text{ cm}^{-1}$. This difference mode contribution vanishes for low temperatures and can be neglected at 10 K. Though, at RT this mode is easily observable at about 90 cm^{-1} [10] and is hence labeled A-DM (difference mode). Its intensity is then comparable to the TO and LO mode and its origin involves various optical and TA phonons.

Due to the strong broadening, most features are only observable up to about 100 K or 200 K, respectively. The energy as a function of temperature is shown for all respective features in figure 3.

We assign the features A₁ and A₄ as difference modes. This assignment was supported by the observed temperature dependencies of their intensities [45, 46]. The structure D shifts twice as fast as the fundamental TO and LO modes, as expected for overtone and combination modes.

With the known origin of the features (table 1) and their temperature dependence, the temperature dependence of acoustic phonons can be determined, which are otherwise not accessible via first-order Raman scattering. The energy of the TA phonons at the L- and X-point is given by their overtones represented by feature A₂ and A₃ respectively. The LA_X phonon can be related to B₁–A₃/2 while LA_L is related to B₃/2.

Before the acoustic phonons' temperature dependence is derived, the impact of the lattice expansion and the phonon–phonon interaction on the properties of the optical phonons at the Γ -point is shortly discussed. This will later support the validity of derived anharmonic contributions, observed in the shifts of acoustic phonons.

Table 3. Fit parameters obtained via equation (2) and S1 (the fits are shown in the supplementary). For these parameters, Klemens-like recombination channels were always assumed ($\omega_i \approx \omega_0/2$). Errors are indicated below respective values. All quantities are given in cm^{-1} .

Mode	ω_0	ω_i	ω_j	Δ_3	Δ_4	Γ_3	Γ_4
TO $_{\Gamma}$	133.3 ± 0.1	67	45	-1.26 ± 0.1	-0.013 ± 0.01	0.36 ± 0.06	0.17 ± 0.01
LO $_{\Gamma}$	150.2 ± 0.2	75	50	-1.1 ± 0.2	0 ± 0.02	0.9 ± 0.15	0.18 ± 0.02

3.3. Optical phonons

The fundamental TO and LO phonons at the Γ -point were analyzed by means of Lorentzian functions. This data (shown in the supplementary) was described by the Klemens model, in which the Raman shift and the mode broadening are related to harmonic effects of the crystal lattice and anharmonic phonon–phonon interactions, i.e. one phonon decays into multiple other phonons [47–49].

Considering contributions from the lattice expansion and the decay of phonons into up to three phonons, the Raman shift of the phonon mode as a function of temperature can be described by [9, 48–50]:

$$\omega(T) = \omega_0 - \Delta_{\text{Lat}}(T) + \Delta_{3\text{ph}}(T) + \Delta_{4\text{ph}}(T) \quad (2)$$

where ω_0 is the unperturbed phonon energy, $\Delta_{3\text{ph}}$, $\Delta_{4\text{ph}}$ are the anharmonic phonon decay processes involving 3 or 4 phonons respectively and Δ_{Lat} is the Raman shift of the phonon due to thermal expansion of the crystal lattice, which is given in detail by [9, 48, 50]:

$$\Delta_{\text{Lat}}(T) = 3\omega_0\gamma \int_0^T \alpha(T') dT'. \quad (3)$$

Here γ denotes the Grüneisen parameter and α the temperature-dependent coefficient of the thermal expansion. The temperature dependence of the thermal expansion coefficient was taken from [51] (see supplementary).

The contributions of the anharmonic processes are described by [47, 49, 50]:

$$\Delta_{3\text{ph}}(T) = \Delta_3 \left[1 + \sum_{i=1}^2 n(\omega_i) \right] \Delta_{4\text{ph}}(T) = \Delta_4 \left[1 + \sum_{j=1}^3 n(\omega_j) + n^2(\omega_j) \right] \quad (4)$$

with Δ_3 and Δ_4 as zero-temperature renormalization constants describing the strength of the individual contributions to the Raman shift. The Grüneisen parameters γ of the respective phonon modes were taken from [10] with $\gamma(\text{TO}_{\Gamma}) = 1.8$ and $\gamma(\text{LO}_{\Gamma}) = 2.5$. This is in accordance with other results [52, 53]. Our calculated Grüneisen parameter band structure is shown in the supplementary and indicates comparable values. For the description of the mode broadening, a similar model is used. Here the parameters Γ_3 and Γ_4 were used, which describe the 3- and 4-phonon processes, respectively [47, 48] (see supplementary). This model fits nicely with our experimental data for the Raman shifts as well as the experimentally determined broadening. The general behavior is quite similar for the TO and LO modes.

For both modes, the Raman shifts are dominated by the 3-phonon process, including a weaker lattice contribution. This lattice contribution matches quite exactly the PBEsol calculations for the LO mode, while for the TO mode a deviation is observed. Nevertheless, the trend is well resembled. A weak contribution of the 4-phonon process is found for the TO mode only.

The fit parameters describing the Raman shift and broadening of the TO and LO mode in table 3 are in agreement with the earlier results from [10] (under consideration of isotope effect and neglected lattice expansion) and as well with [9] (considering the investigated temperature range). A detailed discussion is given in the supplementary.

The PBEsol results for the mode shift as a function of temperature of the TO and LO modes are much lower than the experimentally observed shift of the phonon modes. However, their contribution is approximately equal to the lattice contribution, which was calculated by the individual Grüneisen parameters (from [10], derived via linear response method within DFT) and the experimental coefficient of thermal expansion (from [51]). We use a quasi-harmonic model which only accounts for volume expansion to compute the frequency shift. Therefore, it is not surprising at all, that we only capture this effect. Hence, the PBEsol results can be associated with the lattice expansion contribution.

Overall the analysis with the Klemens model [47] showed, that the 3- and 4-phonon processes and the lattice expansion contribution are relevant for the renormalization and the broadening of the respective

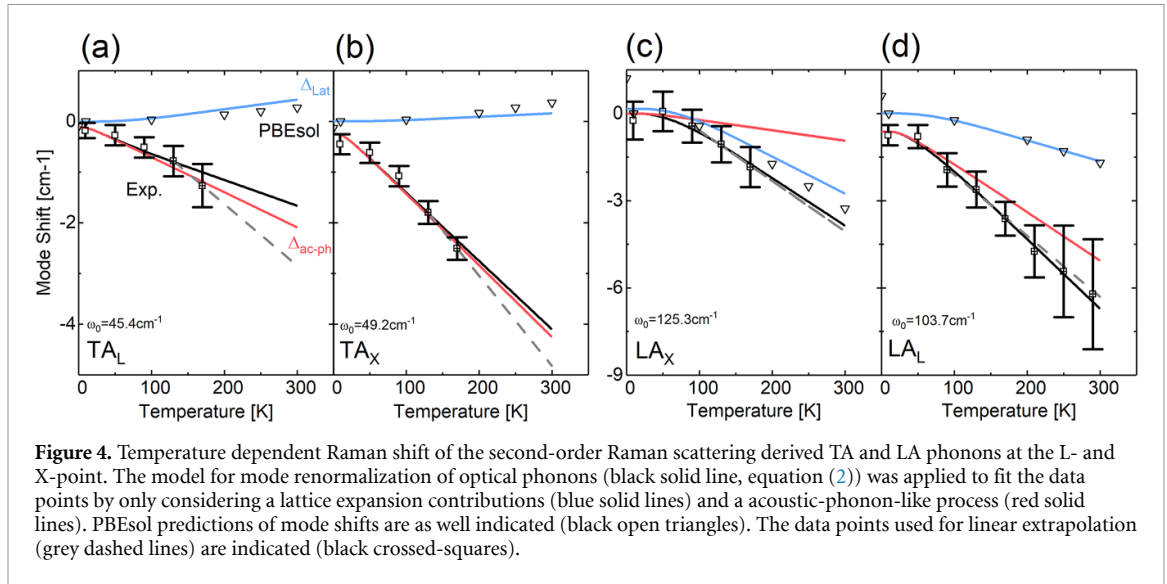


Figure 4. Temperature dependent Raman shift of the second-order Raman scattering derived TA and LA phonons at the L- and X-point. The model for mode renormalization of optical phonons (black solid line, equation (2)) was applied to fit the data points by only considering a lattice expansion contributions (blue solid lines) and a acoustic-phonon-like process (red solid lines). PBESol predictions of mode shifts are as well indicated (black open triangles). The data points used for linear extrapolation (grey dashed lines) are indicated (black crossed-squares).

Table 4. Fit parameters (equation (2)) of acoustic phonons energetic temperature dependence. ω_0 is the unperturbed phonon energy, ω_i the phonon energy of 3-phonon process like contribution and Δ_3 the zero-temperature renormalization constant.

Mode	ω_0	ω_i	Δ_{ac-ph}
TA _L	45.4	23	−0.11
TA _X	49.2	25	−0.25
LA _L	103.7	52	−0.63
LA _X	125.3	62	−0.16

phonon modes. This is in accordance with other publications [9, 10]. The lattice expansion contribution is quite well resembled by the quasi-harmonic model using PBESol. This fact will be used for the identification and validation of harmonic and anharmonic contributions observed in the renormalization of acoustic phonons.

3.4. Acoustic phonons

The experimentally determined TA_L, TA_X, LA_L and LA_X phonon energies at the respective temperature are shown in figures 4(a)–(d). The experimental data for the LA_L mode shows a linear dependence, in agreement with results for other materials like Ge and NaI from [54–56]. The shift of the acoustic phonons from 10 K up to RT is in the range of 2–6 cm^{−1} and is significantly smaller compared to the shifts of the optical ones.

The model by Klemens is only valid for zone-center optical phonons [47]. The observed shifts of the acoustic TA and LA phonons at the L and X point look in principle similar to the ones observed for the TO and LO phonons. Hence, we adapt this for a phenomenological description by including the known lattice expansion and Grüneisen parameters for the respective phonons at the critical points [10] ($\gamma(\text{TA}_L) = -0.9$, $\gamma(\text{TA}_X) = -0.3$, $\gamma(\text{LA}_L) = 1.5$ and $\gamma(\text{LA}_X) = 2.2$). An influence due to the choice of Grüneisen parameters can be excluded, because the deviations compared to our derived Grüneisen parameters is negligible (see supplementary). In this way, the chosen model is similar to equation (2), while considering only the 3-phonon process (decay into two phonons), i.e. $\Delta_4 = 0$. This results in a linear dependence and was sufficient to describe the observed experiment data. To account for other linear processes in Δ_3 , we rename it to Δ_{ac-ph} . This now represents all anharmonic acoustic-phonon contributions. The lattice expansion contribution is included with the respective Grüneisen parameter. The ω_i values are chosen, as before for the optical phonons, as approximately the half of the respective acoustic phonon energy.

The model is shown as well in figures 4(a)–(d) as solid line. The respective parts of lattice expansion (blue) and the contributions from the acoustic-phonon process (red) are shown. The PBESol prediction of the mode shift is also indicated (black triangles), which coincides well with the predicted lattice contribution, as before for the optical modes. A linear extrapolation of the experimental data (dashed grey lines) shows negligible deviations compared to the model, especially for the LA phonons (i.e. $\lesssim 1$ cm^{−1}). This validates the extrapolated RT values for phonon energies of the TA_L, TA_X and LA_X modes. An extrapolation of the LA_X mode data points at higher temperatures can be done using the B₁ feature and the linear extrapolation of the A₃ feature. This agrees with the linear model up to RT. The unperturbed phonon energies are indicated by ω_0 and listed in table 4.

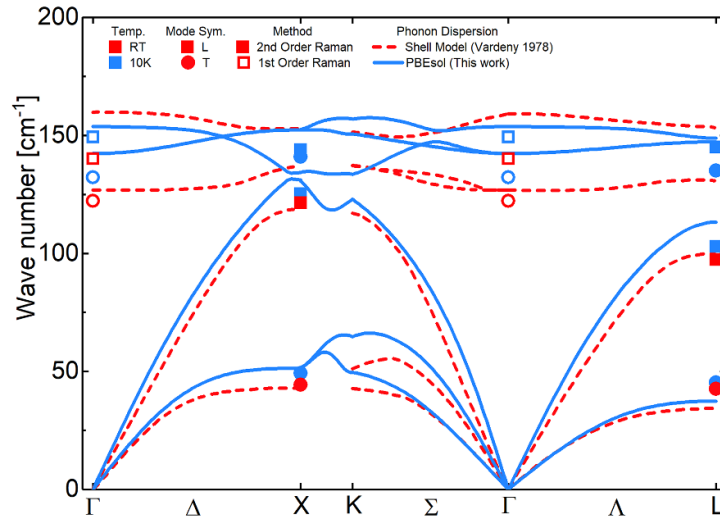


Figure 5. Phonon dispersion along high symmetry directions from the shell model [39] (red dashed line, $T = \text{RT}$) and our PBEsol results (blue line, $T = 10 \text{ K}$). Our experimental data from first- and second-order Raman scattering (open and full symbols). Red colors indicates RT and blue colors indicate a temperature of 10 K. Longitudinal modes are indicated by squares and transversal ones with circles. Note the known significant deviations between Raman data and shell model (red dashed lines) for the TA_L and LO_Γ modes [17–19, 39].

The validity of the model is indicated by a linear extrapolation, as shown in figure 4 (dashed grey line). Compared to the model fit, the linear extrapolation is almost identical for the LA phonons, while slight deviations are observed for the TA phonons (deviation at RT $\lesssim 1 \text{ cm}^{-1}$).

The model describes the experimentally observed behavior quite well. Only the TA modes show slight deviations at low temperatures. This could be linked to possible 3-phonon decay channels, which exist for the LA phonon ($\text{LA} \rightarrow \text{TA} + \text{TA}$) but not for TA phonons [32]. For the TA phonons, only elastic interactions with thermal phonons can be expected [54]. The lattice contribution is negative for the TA mode, as observed for other zincblende semiconductors and is a consequence of the negative Grüneisen parameter [10, 52]. Its effect is quite small compared to the acoustic-phonon contribution and negligible for the TA_X mode. The mode shifts for the TA and LA modes at both critical points are comparable in magnitude. The lattice contribution plays a considerable role for the LA modes, whereby it dominates for the LA_X mode.

The relative deviations by the calculated lattice contribution and the quasi-harmonic contribution from the PBEsol calculations are significantly smaller for the longitudinal phonons than for the transversal phonons. The same trend is observed for the optical phonons and may be related to the transversal characteristics of the respective phonon modes. However, the absolute deviations are negligible and hence the lattice contribution is quite well resembled by the PBEsol theory.

Under consideration of the uncertainties, the extrapolated and observed Raman shifts of the acoustic phonon modes at RT are in agreement with the results of the neutron scattering measurements from [17], except for the TA_L mode. We predict a value of 43 cm^{-1} at RT, which is significantly larger than 34 cm^{-1} [17] (neutron scattering) or 32 cm^{-1} [19] (linear extrapolation from pressure dependence of the rhombohedral phase). For the neutron scattering measurements, this deviation is slightly larger than the given uncertainties. We also note the significant overestimation of the LO phonon energy from neutron scattering compared to Raman spectroscopy measurements [57]. This may explain the large deviation observed for the TA_L mode.

Our determined TA mode positions and shifts can be supported by two different facts. Firstly, by comparing the linear extrapolation with inelastic neutron scattering measurements of CuI [52] (see supplementary). In this reference, a peak structure is observed at about 40 cm^{-1} , which we associate with the TA modes at L- and X-point. Secondly, by considering the temperature dependence of the phonons for the halide group semiconductor CuBr. The relative shifts of the TA phonons for CuBr are matching quite well to the observed relative shifts of the TA phonons of CuI [58].

Our determined LA mode positions and shifts agree well for the L-point, while for the X-point some deviations are observed. The $[\text{LO-LA}]_L$ difference mode observed at 43 cm^{-1} ([59]) as well as the relative shifts for the CuBr [58] support the LA_L assignment. Our observed relative shift for the LA_X mode is only 4% and hence lower than the relative shift of CuBr's LA_X mode with 14% [58]. The strong background signal at the B structure may reason an underestimation of the LA_X mode shift.

These results of our determined optic and acoustic phonon frequencies are summed up in figure 5 and validate the observed temperature trend of both TA phonons and the LA_L phonons with measurements

down to about 10 K. Especially at elevated temperatures the linear trend is observed for all acoustic phonons up to RT. A model including lattice expansion and acoustic phonon processes could be used to describe this behavior. This seems to be valid at least up to RT and possibly as well above [52]. This is also consistent with CuI's high predicted and observed anharmonicity [5, 9, 10], which manifests as well in the characteristics of the acoustic phonons.

4. Summary

We analyzed the anharmonic contributions for acoustic phonons by second-order Raman measurements and DFT-based calculations. This was done exemplarily on bulk single crystals for the p-type semiconductor CuI. Via Raman measurements the fundamental TO and LO modes and 19 second-order Raman features were observed. By means of the DFT-based calculated 2-phonon density of states, the measured spectral shape was well reproduced and each second-order feature was assigned to a two-phonon mode. This allowed us to derive the energy of acoustic phonons in addition to their energetic temperature dependence.

In this way, the CuI's acoustic phonon energies were determined down to 10 K by using a Raman setup, with much higher accuracy than the up to now available neutron scattering results. The known systematic deviation in these neutron scattering measurements, do not extend towards the determined acoustic phonon energies. Only for the TA_L phonon mode we determined a significant different energy.

The TO and LO phonons were analyzed by a Klemens model including harmonic lattice contributions. The latter were additionally verified by using DFT computations and extended for the acoustic phonons to determine their anharmonic contributions. Here the difference between experimental observed mode shift and predicted harmonic shift was assigned to the anharmonic contributions of the respective acoustic phonons. These anharmonicities dominate for most acoustic phonons, similar to the zone-center optical phonons. This trend is mostly linear and extends up to at least RT. Hence, a 3-phonon decay or the elastic thermal phonon scattering may be considered as relevant phonon–phonon interaction processes.

These findings are in agreement with earlier results and extend CuI's determined acoustic phonon properties to lower temperatures with higher accuracy. This approach as well shows that it is possible to characterize the acoustic anharmonicities via Raman scattering.

Data availability statement

The data that support the findings of this study are available upon request from the authors. The data cannot be made publicly available upon publication because they are not available in a format that is sufficiently accessible or reusable by other researchers. The data that support the findings of this study are available upon reasonable request from the authors.

Acknowledgments

We thank Evgeny Krüger for discussion and Lukas Trefflich as well as Gabriele Benndorf (both from the University of Leipzig) for technical support. We gratefully acknowledge funding from the Deutsche Forschungsgemeinschaft (DFG, German Research Foundation) through FOR 2857 - 403159832. Furthermore we acknowledge the Leibniz Supercomputing Center for granting computational resources (Project No. pn68le). R H acknowledges the Leipzig School of Natural Sciences BuildMoNa.

ORCID iDs

R Hildebrandt  <https://orcid.org/0000-0001-6932-604X>

M Seifert  <https://orcid.org/0000-0002-4397-0125>

J George  <https://orcid.org/0000-0001-8907-0336>

S Botti  <https://orcid.org/0000-0002-4920-2370>

H Krautscheid  <https://orcid.org/0000-0002-5931-5440>

M Grundmann  <https://orcid.org/0000-0001-7554-182X>

C Sturm  <https://orcid.org/0000-0001-8664-236X>

References

- [1] Pagès O, Tite T, Kim K, Graf P A, Maksimov O and Tamargo M C 2006 *J. Phys.: Condens. Matter* **18** 577–95
- [2] Bai Z, He D, Fu S, Miao Q, Liu S, Huang M, Zhao K, Wang Y and Zhang X 2022 *Nano Sel.* **3** 1112–22
- [3] Aksamija Z and Ravaioli U 2009 *J. Phys.: Conf. Ser.* **193** 012033
- [4] Kirchartz T, Markvart T, Rau U and Egger D A 2018 *J. Phys. Chem. Lett.* **9** 939–46

- [5] Knoop F, Purcell T A R, Scheffler M and Carbogno C 2023 *Phys. Rev. Lett.* **130** 236301
- [6] Coroa J, Morais Faustino B M, Marques A, Bianchi C, Koskinen T, Juntunen T, Tittonen I and Ferreira I 2019 *RSC Adv.* **9** 35384–91
- [7] Schmidl G, Jia G, Gawlik A, Lorenz P, Zieger G, Dellith J, Diegel M and Plentz J 2022 *Materials* **16** 13
- [8] Wei B, Sun Q, Li C and Hong J 2021 *Sci. China Phys. Mech. Astron.* **64** 117001
- [9] He H and Zhang Z 2019 *AIP Adv.* **9** 055104
- [10] Serrano J, Cardona M, Ritter T M, Weinstein B A, Rubio A and Lin C T 2002 *Phys. Rev. B* **66** 245202
- [11] Yang C, Souchay D, Kneiß M, Bogner M, Wei H M, Lorenz M, Oeckler O, Benstetter G, Fu Y Q and Grundmann M 2017 *Nat. Commun.* **8** 16076
- [12] Krüger E et al 2021 *APL Mater.* **9** 121102
- [13] Chen D, Wang Y, Lin Z, Huang J, Chen X, Pan D and Huang F 2010 *Cryst. Growth Des.* **10** 2057–60
- [14] Lin W et al 2018 *ACS Appl. Mater. Interfaces* **10** 43699–706
- [15] Liu A, Zhu H, Park W T, Kim S J, Kim H, Kim M G and Noh Y Y 2020 *Nat. Commun.* **11** 4309
- [16] Baek S D, Kwon D K, Kim Y C and Myoung J M 2020 *ACS Appl. Mater. Interfaces* **12** 6037–47
- [17] Hennion B, Moussa F, Prevot B, Carabatos C and Schawb C 1972 *Phys. Rev. Lett.* **28** 964–6
- [18] Prevot B and Sieskind M 1974 *Phys. Status Solidi b* **61** 121–4
- [19] Brafman O, Cardona M and Vardeny Z 1976 *Phys. Rev. B* **15** 1081–6
- [20] Hardt D and Bollig R 1965 *Angew. Chem.* **77** 860
- [21] Gao P, Gu M, Liu X, Yang C F, Zheng Y Q and Shi E W 2013 *CrystEngComm* **15** 2934
- [22] Kresse G and Furthmüller J 1996 *Comput. Mater. Sci.* **6** 15–50
- [23] Kresse G and Joubert D 1999 *Phys. Rev. B* **59** 1758–75
- [24] Blöchl P E 1994 *Phys. Rev. B* **50** 17953–79
- [25] Seifert M, Kawashima M, Rödl C and Botti S 2021 *J. Mater. Chem.* **9** 11284–91
- [26] Seifert M, Krüger E, Bar M S, Merker S, von Wenckstern H, Krautscheid H, Grundmann M, Sturm C and Botti S 2022 *Phys. Rev. Mater.* **6** 124601
- [27] Pallikara I, Kayastha P, Skelton J M and Whalley L D 2022 *Electron. Struct.* **4** 033002
- [28] Perdew J P, Ruzsinszky A, Csonka G I, Vydrov O A, Scuseria G E, Constantin L A, Zhou X and Burke K 2008 *Phys. Rev. Lett.* **100** 136406
- [29] Togo A, Oba F and Tanaka I 2008 *Phys. Rev. B* **78** 134106
- [30] Togo A and Tanaka I 2015 *Scr. Mater.* **108** 1–5
- [31] Stoffel R P, Wessel C, Lumey M W and Dronskowski R 2010 *Angew. Chem., Int. Edn.* **49** 5242–66
- [32] Okubo K and Tamura S I 1983 *Phys. Rev. B* **28** 4847–50
- [33] Birman J L 1963 *Phys. Rev.* **131** 1489–96
- [34] Cardona M, Güntherodt G, Chang R K, Long M B and Vogt H 1981 *Light Scattering in Solids II: Basic Concepts and Instrumentation* 1st edn (Springer)
- [35] Loudon R 2001 *Adv. Phys.* **50** 813–64
- [36] Irwin J C and LaCombe J 1970 Second-order Raman spectrum of ZnSe *Can. J. Phys.* **48** 2499–506
- [37] Vagelatos N, Wehe D and King J S 1974 *J. Chem. Phys.* **60** 3613–8
- [38] La Combe J L 1971 Raman studies of phonon dispersion in zincblende semiconductors *Dissertation* Simon Fraser University Burnaby Canada (available at: https://summit.sfu.ca/_flysystem/fedora/sfu_migrate/4386/b13732316.pdf)
- [39] Vardeny Z, Gilat G and Moses D 1978 *Phys. Rev. B* **18** 4487–96
- [40] Johnson F A and Loudon R 1964 *Proc. R. Soc. A* **281** 274–90
- [41] Plendl J N, Hadni A, Claudel J, Henninger Y, Morlot G, Strimer P and Mansur L C 1966 *Appl. Opt.* **5** 397–401
- [42] Keyes R W 1962 *J. Chem. Phys.* **37** 72–73
- [43] Mitra S S 1963 *Phys. Rev.* **12** 986–91
- [44] Petretto G et al 2018 *Sci. Data* **5** 180065
- [45] Potts J E, Walker C T and Nair I R 1972 *Phys. Rev. B* **8** 2756–71
- [46] Weber W H and Merlin R 2000 *Raman Scattering in Materials Science* (Springer)
- [47] Klemens P G 1966 *Phys. Rev.* **148** 845–8
- [48] Giehler M, Ramsteiner M, Waltereit P, Brandt O, Ploog K H and Obloh H 2001 *J. Appl. Phys.* **89** 3634–41
- [49] Balkanski M, Wallis R F and Haro E 1983 *Phys. Rev. B* **28** 1928–34
- [50] Tristant D, Cupo A, Ling X and Meunier V 2019 *ACS Nano* **13** 10456–68
- [51] Nakamura M, Inagaki S, Okamura Y, Ogino M, Takahashi Y, Adachi K, Hashizume D, Tokura Y and Kawasaki M 2022 *Phys. Rev. B* **106** 125307
- [52] Gopakumar A M, Gupta M K, Mittal R, Rols S and Chaplot S L 2017 *Phys. Chem. Chem. Phys.* **19** 12107–16
- [53] Plendl J N and Mansur L C 1972 *Appl. Opt.* **11** 1194–9
- [54] Kulda J, Debernardi A, Cardona M, de Geuser F and Haller E E 2004 *Phys. Rev. B* **69** 045209
- [55] Li F, Shen J, Parnell S R, Thaler A N, Matsuda M, Keller T, Delaire O, Pynn R and Fernandez-Baca J A 2019 *J. Appl. Crystallogr.* **52** 755–60
- [56] Kempa M, Ondrejovic P, Bourges P, Ollivier J, Rols S, Kulda J, Margueron S and Hlinka J 2013 *J. Phys.: Condens. Matter* **25** 055403
- [57] Potts J E, Hanson R C, Walker C T and Schwab C 1973 *Solid State Commun.* **13** 389–92
- [58] Hoshino S, Fujii Y, Harada J and Axe J D 1976 *J. Phys. Soc. Japan* **41** 965–73
- [59] Livescu G and Brafman O 1986 *J. Phys. C: Solid State Phys.* **19** 2663